

# How Oxygen Absorption Affects the Al<sub>2</sub>O<sub>3</sub>-Encapsulated Blue Phosphorene–Au Alloy

Gabriele Faraone, Christian Martella, Emiliano Bonera, Alessandro Molle,\* and Carlo Grazianetti


The urgent quest to introduce the Xenes, a new family of graphene-like materials, into everyday technological devices furthers demands for a specific understanding of their reactivity to different environments. Herein, the role of oxygen on blue phosphorene fragments alloyed with the Au(111) substrate, the so-called BlueP–Au alloy, is investigated both on a microscopic scale and at the interface with Al<sub>2</sub>O<sub>3</sub>, commonly used to protect Xenes in ambient conditions. Although molecular oxygen does not affect the BlueP–Au alloy or intercalate below it, the role of oxygen is fundamental to relieve the charging effects at the very interface between Al<sub>2</sub>O<sub>3</sub> and the BlueP–Au alloy when exposed to air. These findings highlight the importance of combining different tools, including microscopy and spectroscopy, to ascertain the stability of 2D materials in device-ready configurations.

## 1. Introduction

The Xenes are today an emerging 2D-material family including artificial graphene-like materials discovered soon after the isolation of their carbon-based progenitor.<sup>[1]</sup> Among them, the honeycomb lattices made of elements of the column IVA (below carbon) have attracted much interest because of their potential applications in the electronics industry, such as silicon and germanium, or for recent outcomes related to topological physics, such as tin.<sup>[2–4]</sup> Xene-like silicene, germanene, and stanene show properties akin to graphene and the increasing mass of the X element from carbon to tin enables the opening of a bandgap due to spin–orbit coupling effects, e.g., up to 0.3 eV for stanene

Dr. G. Faraone, Dr. C. Martella, Dr. A. Molle, Dr. C. Grazianetti  
CNR-IMM Unit of Agrate Brianza  
via C. Olivetti 2, Agrate Brianza I-20864, Italy  
E-mail: alessandro.molle@mdm.imm.cnr.it

Dr. G. Faraone, Prof. E. Bonera  
LNESS and Dipartimento di Scienza dei Materiali  
Università degli Studi di Milano Bicocca  
Via Cozzi-55, I-20125 Milano, Italy

 The ORCID identification number(s) for the author(s) of this article can be found under <https://doi.org/10.1002/pssr.202100217>.

© 2021 The Authors. physica status solidi (RRL) rapid research letters published by Wiley-VCH GmbH. This is an open access article under the terms of the Creative Commons Attribution License, which permits use, distribution and reproduction in any medium, provided the original work is properly cited.

DOI: 10.1002/pssr.202100217

on Cu(111),<sup>[5]</sup> compatible with technological applications, especially in the electronics field, where graphene suffers from intrinsic limitations.<sup>[1]</sup> Another route to reach out the same goal, i.e., bandgap opening, is looking at neighbor elements of the IVA column. In this framework, the exfoliation of black phosphorus, the most stable allotrope of phosphorus, resulted in a new 2D material called “phosphorene.”<sup>[6]</sup> Similar to graphene, phosphorene obtained from mechanical exfoliation also possesses a counterpart called blue phosphorene (or blue phosphorus in its layered form), which does not exist in nature, as predicted by theoretical calculations.<sup>[7]</sup> The structure of blue phosphorene is closer to silicene than black phosphorene and its bandgap

decreases from 2 eV in the single layer to  $\approx 1.2$  eV for the bulk.<sup>[7]</sup> The first attempts to artificially create blue phosphorene were based on molecular beam epitaxy (MBE) of evaporated black phosphorus on a metallic substrate, i.e., Au(111), following avenues traced by silicene on Ag(111).<sup>[8]</sup> Although the experimental results achieved by Zhang et al. were successfully replicated by other groups,<sup>[9–13]</sup> some inconsistencies in the blue phosphorene structure arrangement on Au(111) eventually led to the conclusion that blue phosphorene fragments are alloyed with gold atoms of the templates.<sup>[14,15]</sup> Nonetheless an encapsulation and transfer process for blue phosphorene fragments alloyed with gold atoms (hereafter BlueP–Au alloy) has been already developed and is based on the BlueP–Au alloy being sandwiched in between an Al<sub>2</sub>O<sub>3</sub> capping layer (as for other Xenes)<sup>[16]</sup> and thin gold films on mica.<sup>[9]</sup> Intriguingly, freestanding-like blue phosphorene can be successfully synthesized by means of silicon intercalation of the BlueP–Au alloy.<sup>[17]</sup> A similar intercalation mechanism (by means of oxygen) has been already reported for silicene on Ag(111), thus resulting in a quasi-free-standing silicene.<sup>[18]</sup> Nonetheless, the BlueP–Au alloy system is also interesting as an intriguing example of the metal–phosphorus networks (inspired by the so-called metal–organic networks) that, in this specific case, can be artificially grown by MBE.<sup>[14]</sup> In light of these considerations and the proven air instability of the BlueP–Au alloy when exposed to ambient conditions,<sup>[9]</sup> here the role of molecular oxygen on the atomic structure of the BlueP–Au alloy as well as the role of air in the electrostatics at the Al<sub>2</sub>O<sub>3</sub>/BlueP–Au alloy interface are investigated to find viable routes for blue phosphorene synthesis and encapsulation aiming at real-world applications.

## 2. Role of Oxygen Molecules in BlueP–Au Alloy

In the framework of the chemical stability of Xenes, the oxidation of silicene grown on Ag(111) was initially studied through X-ray photoelectron spectroscopy (XPS) and only recently Du et al. investigated the molecular oxygen's role in the intercalation on bilayer silicene islands on the same substrate.<sup>[18,19]</sup> Recently we demonstrated via XPS that in the case of BlueP–Au alloy grown by MBE on Au(111) thin films on mica (see Experimental Section), the chemical reactivity upon oxygen exposure is very low.<sup>[9]</sup> However, a microscopic characterization to elucidate the possible intercalation of molecular oxygen with oxygen doses comparable with those used by Du et al. (up to 1200 L) has not been reported yet. Reversible oxidation on the BlueP–Au alloy was already investigated with higher doses (>18 000 L) to study the fundamental pathways of the degradation mechanism.<sup>[20]</sup> **Figure 1a** shows the characteristic flower-like pattern of the BlueP–Au alloy observed by scanning tunneling microscopy (STM).<sup>[9]</sup> This pattern is originated by blue-phosphorene subunits coaxed together with gold atoms, thus forming a 2D ordered network on the Au(111) surface.<sup>[14]</sup> **Figure 1b** shows the same surface after 2000 L of molecular oxygen exposure where clusters with different heights and dimensions can be observed (compare the line profiles in **Figure 1a** with those in **Figure 1b** taken before and after the exposure to O<sub>2</sub>). As highlighted by the line profiles in **Figure 1a,b**, the typical height of the clusters above each blue-phosphorene subunit lies between 1 and 2 Å. Although the atomic structure of the larger clusters can be hardly accessed by STM investigation, the topographic image in **Figure 1b** shows also the presence of small bright spots (denoted by red arrows) located at various positions on the triangular-shaped petals of the flowerlike BlueP–Au alloy

pattern, which can be identified as oxygen atoms adsorbed on the surface, as already reported in the literature.<sup>[20]</sup>

## 3. Role of Oxygen in Al<sub>2</sub>O<sub>3</sub>-Encapsulated BlueP–Au Alloy

Even if the STM analysis proves that the BlueP–Au alloy is unaffected by in situ doses of molecular oxygen, when exposed to dry air the BlueP–Au alloy undergoes oxidation.<sup>[9]</sup> A viable option enabling to take the BlueP–Au alloy out of an ultrahigh vacuum (UHV) environment is growing a capping layer on top. We already demonstrated that a thin layer made of Al<sub>2</sub>O<sub>3</sub> can hinder the oxidation of the underlying Xenes and of the BlueP–Au alloy as well.<sup>[9,16]</sup> The Al<sub>2</sub>O<sub>3</sub> capping does not alter the chemical stability of the BlueP–Au alloy outside the growth environment as well as in a wet environment such as the tetrahydrofuran bath, being able to significantly slow down the oxidation process after a prolonged air exposure.

Although stoichiometric, the MBE-grown Al<sub>2</sub>O<sub>3</sub> protection layer is characterized by the presence of fixed intrinsic charges that alter the electrostatic charge-neutrality condition at the Al<sub>2</sub>O<sub>3</sub>/BlueP–Au alloy interface by creating an interfacial space charge region.<sup>[16,19,21]</sup> **Figure 2a** shows the XPS spectra of the Au 4f core levels measured from a reference Al<sub>2</sub>O<sub>3</sub>/Au(111) sample and it can be noted that after Al<sub>2</sub>O<sub>3</sub> deposition the Au 4f core levels are shifted to higher binding energy (of 0.4 eV). An even larger shift (0.7 eV) is also observed after Al<sub>2</sub>O<sub>3</sub> deposition on the BlueP–Au alloy (**Figure 2b**), which turns out to increase the charging effect originally observed in the reference sample. Interestingly, we observe that the Au 4f core levels backshift toward the pristine binding energy (84.0 eV) position when the Al<sub>2</sub>O<sub>3</sub>-capped BlueP–Au alloy samples are exposed to air

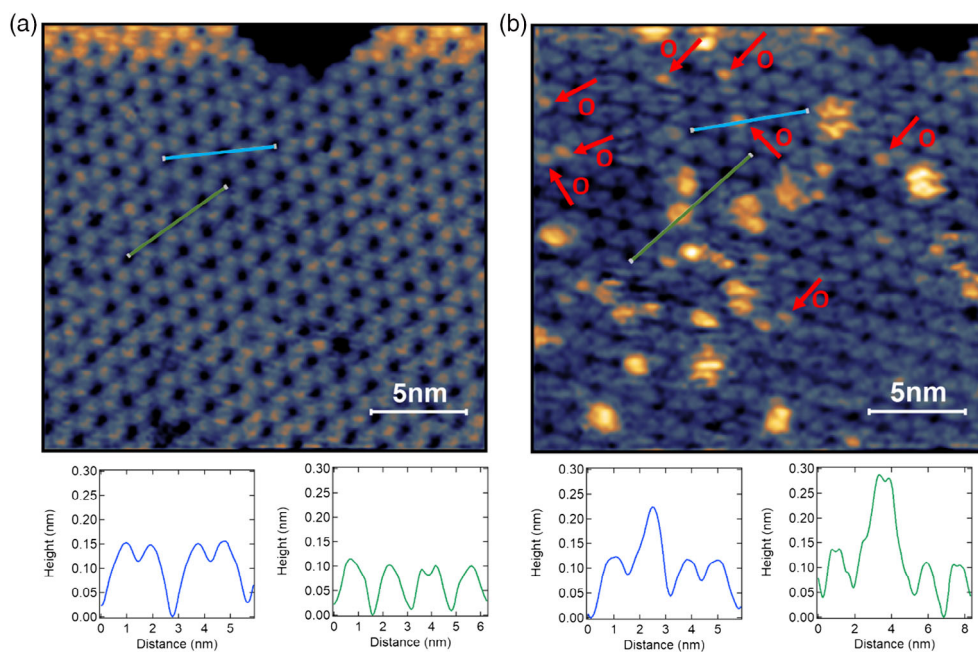


**Figure 1.** a,b) STM images of (20 × 20) nm<sup>2</sup> of the BlueP–Au alloy before (a) and after (b) the exposure to 2000 L of O<sub>2</sub>. STM profiles are reported along the green and blue lines traced in the topographic images.

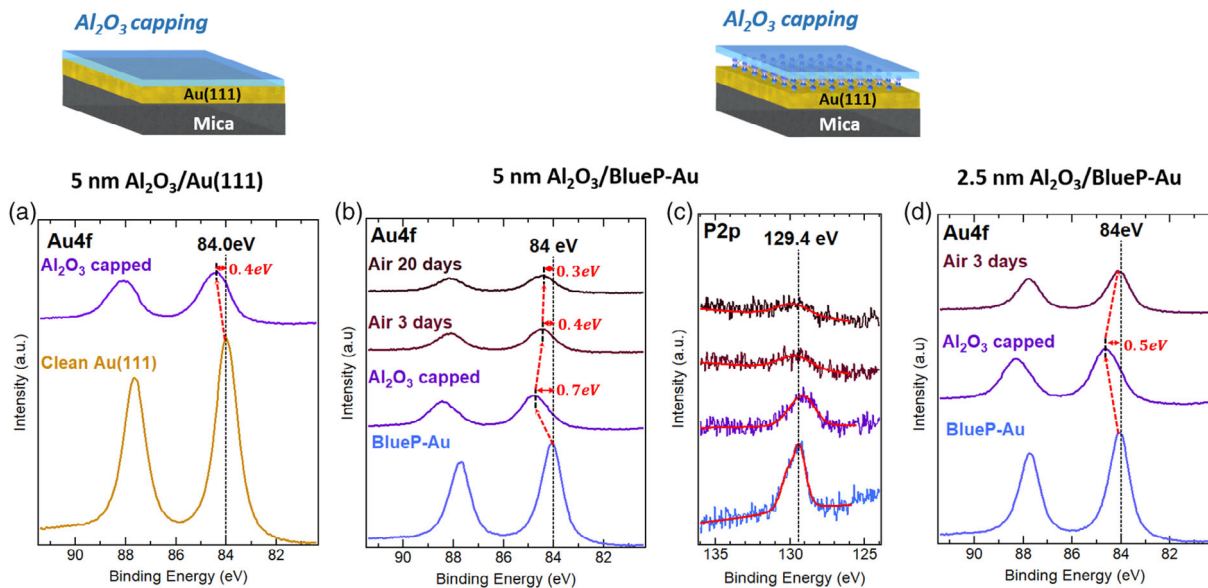


**Figure 2.** a) XPS of the Au 4f core level measured before and after the Al<sub>2</sub>O<sub>3</sub> deposition on an Au(111) reference sample. b) 5 nm-thick Al<sub>2</sub>O<sub>3</sub>-encapsulated BlueP–Au alloy measured after 3 and 20 days of ambient condition exposure. c) P 2p core level as in (b) where modifications of the intensity and background can be attributed to the air exposure (the red lines are fitted curves taking into account the 0.86 eV doublet separation). d) Au 4f core levels as in (b) but with a thinner (2.5 nm) Al<sub>2</sub>O<sub>3</sub> capping layer.

as shown by the dashed arrows in Figure 2b, thus suggesting that oxygen chemisorption in defect sites of the Al<sub>2</sub>O<sub>3</sub> capping layer may induce a partial neutralization of the interfacial space charge region. By comparison, the large shift can be explained by the blue-phosphorene fragments that, even if alloyed with the gold substrate, constitute an additional barrier for the photoemitted electrons of the Au(111) surface, thus resulting in a continuous 2D layer as evidenced by the STM images of Figure 1. On the other hand, the P 2p core level (at 129.3 eV) is unaffected by oxygen incorporation in the Al<sub>2</sub>O<sub>3</sub> capping layer even after months, as reported in Figure 2c, evidencing only a small shift to lower binding energy when the BlueP–Au alloy is capped by Al<sub>2</sub>O<sub>3</sub>. We note that the charging effect is dependent on the capping layer thickness as we observe a comparatively lower binding energy shift (0.5 eV) when the capping layer thickness is reduced down to 2.5 nm (Figure 2d). This behavior can be inherently related to the amount of incorporated fixed charge in the capping layer.

This picture is corroborated by conductive atomic force microscopy (C-AFM) analysis conducted ex situ in contact mode. C-AFM has been applied to map the current leakage under a constant applied bias (2.5 V) through the thin 5 nm thick Al<sub>2</sub>O<sub>3</sub> capping layer both in the Al<sub>2</sub>O<sub>3</sub>/BlueP–Au alloy and in the reference Al<sub>2</sub>O<sub>3</sub>/Au(111); see sketch in Figure 3. The results of this analysis for the Al<sub>2</sub>O<sub>3</sub>/BlueP–Au alloy sample are reported in Figure 3b,c. From the current maps we note that the Al<sub>2</sub>O<sub>3</sub> surface, although uniform in the topographic image (Figure 3b), is characterized by the appearance of isolated spots of high electrical conductivity (bright yellow regions in Figure 3c). These regions are present in both samples, thus suggesting not only that the Al<sub>2</sub>O<sub>3</sub>, albeit stoichiometric, has a defective nature, but also that the BlueP–Au alloy does not hinder the formation of electrically conductive paths through the gold substrate and the AFM tip. In this

framework, the artificial engineering of a 2D metal–phosphorus network could be another route to achieving atomic-thin memristors as recently proposed for the MoS<sub>2</sub>–Au case.<sup>[22]</sup> We note that the observed defects of the Al<sub>2</sub>O<sub>3</sub> matrix (oxide defects) may be at the origin of fixed charges at the Al<sub>2</sub>O<sub>3</sub>/BlueP–Au alloy interface.<sup>[21]</sup>

A deeper insight into this aspect is provided by the electrostatic force microscopy (EFM) investigation of both the samples. In the EFM, the electrostatic force acting on the AFM tip induces a shift of the resonance phase condition ( $\Phi$ ) in response to a bias voltage ( $V_g$ ) applied at the Au substrate according to

$$|\tan \Phi| \approx \frac{Q_f}{k} \frac{C(z)}{z^2} V_g^2 \quad (1)$$

where  $Q_f$  and  $k$  are the quality factor and spring constant of the AFM cantilever, respectively, and  $C(z)$  is the electrical capacitance between the substrate and the conductive AFM tip separated by the distance  $z$  (Figure 3a).<sup>[23–25]</sup>

According to Equation (1), the change in the slope of the function  $|\tan(\Phi)|$  versus  $V_g^2$ , reported in Figure 3d, indicates that the electrical capacitance varies more than 10% within the two samples, and in particular  $C(z)$  decreases in the capped BlueP–Au alloy ( $1.10 \times 10^{-19}$  F) compared to the reference sample ( $1.24 \times 10^{-19}$  F). In a simplified picture, these findings hint at a change of the electrical charges induced at the AFM tip ( $C \approx V/Q$ ) because of the electrostatic screening potential of the Al<sub>2</sub>O<sub>3</sub>/BlueP–Au alloy stack. We can speculate that this effect is the result of the competition between the large electronic polarizability expected in atomically thin materials and the presence of free charges connected with oxide defects in the Al<sub>2</sub>O<sub>3</sub> capping layer.<sup>[21,23,26]</sup>

To confirm the surmise that defects in the Al<sub>2</sub>O<sub>3</sub> become preferential adsorption sites for oxygen when the samples are

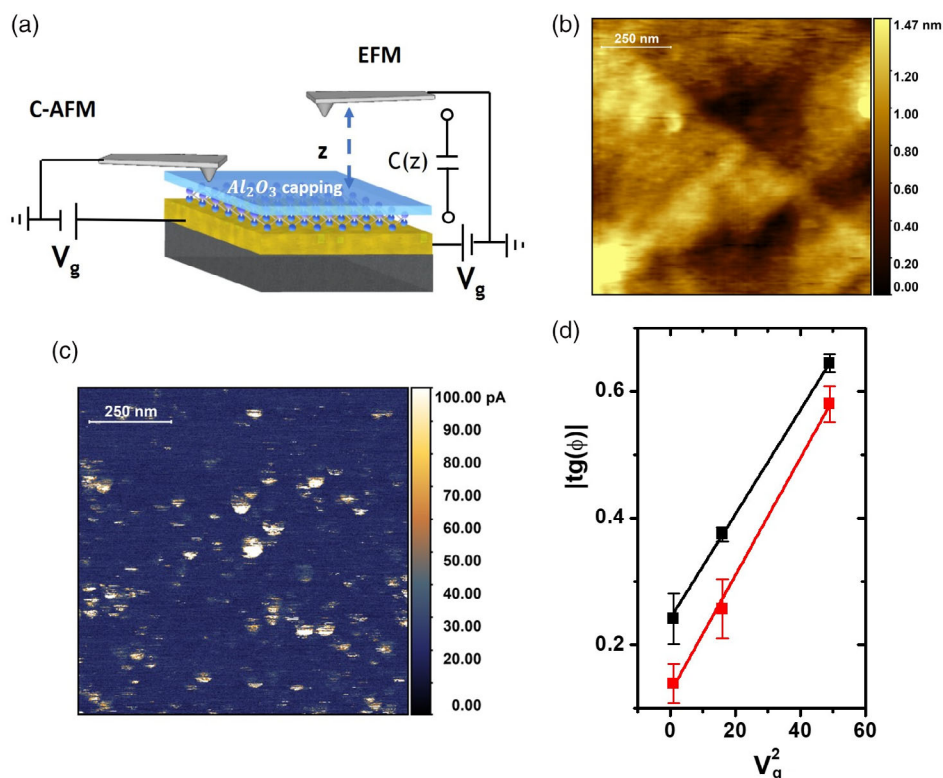


**Figure 3.** a) Schematic view of C-AFM and EFM experiments performed on the  $Al_2O_3$ -encapsulated BlueP-Au alloy. In the C-AFM configuration, the microscope acquires the electrical current flowing between the gold substrate, used as the bottom electrode, and the conductive AFM tip (top electrode) kept in direct contact with the  $Al_2O_3$  capping layer during the scanning of the sample surface. In the EFM configuration, the microscope acquires the phase signal in noncontact mode, i.e., when the AFM tip is at a distance  $z$  respect to the sample surface. b) AFM topography and c) C-AFM image (bias 2.5 V) of  $(1 \times 1) \mu m^2$  area taken on  $Al_2O_3$ /BlueP-Au alloy sample. d) Plot and fit of the  $|tg(\phi)|$  values at different gate voltages for the  $Al_2O_3$ /BlueP-Au alloy (black squares) and  $Al_2O_3$ /Au (red squares) derived from the EFM measurements.

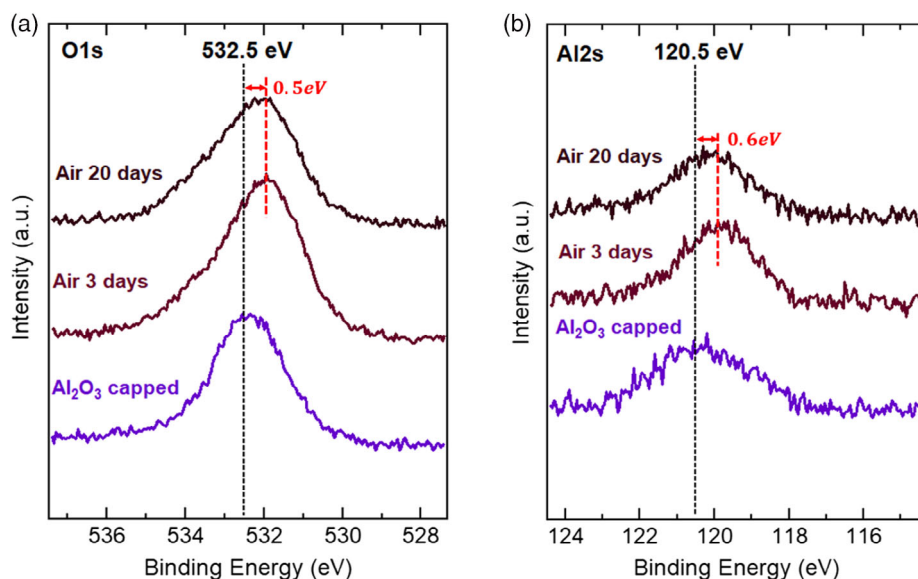


**Figure 4.** a,b) XPS of the O 1s (a) and Al 2s (b) core levels of the BlueP-Au alloy sample measured after the  $Al_2O_3$  growth, 3 and 20 days of exposure to ambient air.

exposed to air, we reintroduced them back in UHV to check the chemical status. Figure 4 reports the XPS core levels of O 1s and Al 2s. The usually scrutinized Al 2p core level is not reported for discussion here because it is very close to the P 2p and therefore affected by its background.<sup>[9]</sup> For a stoichiometric Al<sub>2</sub>O<sub>3</sub> capping layer the O 1s core level is placed at 532.5 eV, whereas Al 2s is at 120.5 eV, i.e., +2.5 eV from the metallic Al state.<sup>[19]</sup> After air exposure and therefore oxygen chemisorption, we observe a rigid shift in both O 1s and Al 2s, nearly comparable with that observed in the Au 4f core levels (see Figure 2b). The O 1s core level shape progressively becomes asymmetric with a tail at higher binding energy (Figure 4a), which can be associated with hydroxyl groups (–OH) adsorption.<sup>[27]</sup> Conversely, the Al 2s core level shows a tail at lower binding energy (see Figure 4b) that is related to a residual metallic component caused by the Al<sub>2</sub>O<sub>3</sub> deposition process, which consists of a predeposition of a first Al layer to prevent oxidation of the underlying Xene.<sup>[16,19]</sup> After 3 days' exposure, both O 1s and Al 2s core levels are shifted to lower binding energy (of 0.5 and 0.6 eV, respectively; see Figure 4) and their binding energy does not change after the 20 day long exposure. It takes up to 20 days instead to progressively restore the pristine binding energy of the Au 4f core levels. On one hand, this behavior explains why this so-grown capping layer is effective to protect the underlying 2D layer, i.e., the charge compensation occurs on a scale of days, but, on the other hand, for specific applications, e.g., electronic devices, developing additional protective layers is highly demanded. Recently, a viable option was proposed by adding an atomic-layer-deposition-made Al<sub>2</sub>O<sub>3</sub> capping layer on top of the amorphous one.<sup>[28]</sup>

## 4. Conclusion

We have elucidated the reactivity of molecular oxygen both on the pristine and on the Al<sub>2</sub>O<sub>3</sub>-encapsulated BlueP–Au alloy surfaces. Our findings indicate that the interaction of molecular oxygen with both the interfaces occurs in different circumstances. Oxygen is chemisorbed on top of the pristine BlueP–Au interface but does not compromise the structural integrity or intercalate through the crystalline structure of the alloy. Conversely, the oxygen incorporation into the Al<sub>2</sub>O<sub>3</sub> matrix-encapsulated BlueP–Au is promoted at oxide defects sites and manifested by a change in the binding energy of the aluminum and oxygen atomic species as measured by XPS. Such an effect satisfactorily accounts for the partial neutralization of the intrinsic fixed charges observed as soon as the as-grown ultrathin Al<sub>2</sub>O<sub>3</sub> oxide is exposed to air. However, a different behavior is observed by comparison between the reference Al<sub>2</sub>O<sub>3</sub>/Au and Al<sub>2</sub>O<sub>3</sub>/BlueP–Au/Au samples. These outcomes show that for real-world applications based on Xenes, a deeper understanding of their chemical reactivity toward ambient environment as well as the electrostatics at the interface with oxide should be taken into account. Moreover, the formation of a metal–phosphorus network, arranged in a crystalline 2D layer, might pave the way to a new class of Xene derivatives with different properties, where Xene fragments alloyed with the hosting metal substrates could be atomically tailored and engineered.

## 5. Experimental Section

**MBE Growth and O<sub>2</sub> Exposure:** Experiments were conducted in a UHV (base pressure 10<sup>–10</sup> mbar) system equipped with three interconnected chambers for sample growth via MBE, chemical analysis via XPS, and morphological characterization via STM. Clean ≈300 nm Au(111)/mica substrates were prepared by repeated Ar<sup>+</sup> bombardment (1 kV, 1 × 10<sup>–6</sup> mbar) and subsequent annealing at 500 °C for 30 min. Phosphorus was deposited by evaporation from a crucible containing bulk black phosphorus. During the deposition process, the substrate temperature was kept in between 240 and 270 °C, thus resulting in BlueP–Au alloy monolayer coverage. The temperature readings were crosschecked by pyrometer-based calibration of the thermocouple attached under the sample holder. An Al<sub>2</sub>O<sub>3</sub> capping layer was grown in situ by codeposition of an aluminum beam from a k-cell and ultrapure molecular oxygen. The Al<sub>2</sub>O<sub>3</sub> thickness was measured ex situ via AFM. Ultrapure O<sub>2</sub> was introduced in the growth chamber by a leak valve at a partial pressure of 1.3 × 10<sup>–6</sup> mbar. The oxygen dose was 2000 L (where 1 L = 1 s at 1.3 × 10<sup>–6</sup> mbar).

**STM and XPS Measurements:** STM images were acquired at room temperature with a homemade tungsten tip precalibrated onto a HOPG surface. STM topographies were typically acquired at –1.3 V and 0.3 nA setpoint. XPS measurements were conducted in situ with nonmonochromatized Mg (1253.6 eV) at a take-off angle of 37°.

**C-AFM and EFM:** Ex situ C-AFM and EFM investigations were conducted with a commercial AFM–Bruker Dimension Edge. For the C-AFM, the microscope was equipped with a tunnelling-AFM electrometer (TUNA) with 1 pA to 1 μA current range. Current maps were acquired in contact mode using highly doped diamond-coated tips (CDT-CONTR, nanosensor) with typical radius of curvature of ≈100 nm. A bias voltage (2.5 V) was applied to the substrate, while the tip was electrically grounded. The EFM investigations were conducted in tapping mode with conductive Pt/Ir-coated tips in a dual pass scan. In the first scan, the topography was acquired with the tip electrically grounded; in the second scan the phase signal was acquired withdrawing the tip at a lift height of 30 nm above the surface and applying a DC electrical signal varied in the range 1–7 V. Note that the dual pass scan hinders artifacts due to topography crosstalk.

## Acknowledgements

The authors acknowledge Mario Alia (CNR-IMM) for technical support and funding support from H2020 ERC CoG 2017 Grant No. 772261 “XFab.”

## Conflict of Interest

The authors declare no conflict of interest.

## Keywords

BlueP–Au alloy, capping layers, molecular beam epitaxy, phosphorene, Xenes

Received: April 19, 2021

Revised: May 20, 2021

Published online: June 26, 2021

[1] C. Grazianetti, C. Martella, A. Molle, *Phys. Status Solidi RRL* **2019**, *14*, 1900439.

[2] C. Grazianetti, A. Molle, *Research* **2019**, *2019*, 1.

[3] A. Acun, L. Zhang, P. Bampoulis, M. Farmanbar, A. van Houselt, A. N. Rudenko, M. Lingenfelder, G. Brocks, B. Poelsema,

- M. I. Katsnelson, H. J. W. Zandvliet, *J. Phys. Condens. Matter* **2015**, *27*, 443002.
- [4] N. Si, Q. Yao, Y. Jiang, H. Li, D. Zhou, Q. Ji, H. Huang, H. Li, T. Niu, *J. Phys. Chem. Lett.* **2020**, *11*, 1317.
- [5] J. Deng, B. Xia, X. Ma, H. Chen, H. Shan, X. Zhai, B. Li, A. Zhao, Y. Xu, W. Duan, S.-C. Zhang, B. Wang, J. G. Hou, *Nat. Mater.* **2018**, *17*, 1081.
- [6] H. Liu, A. T. Neal, Z. Zhu, Z. Luo, X. Xu, D. Tománek, P. D. Ye, *ACS Nano* **2014**, *8*, 4033.
- [7] Z. Zhu, D. Tománek, *Phys. Rev. Lett.* **2014**, *112*, 176802.
- [8] J. L. Zhang, S. Zhao, C. Han, Z. Wang, S. Zhong, S. Sun, R. Guo, X. Zhou, C. D. Gu, K. Di Yuan, Z. Li, W. Chen, *Nano Lett.* **2016**, *16*, 4903.
- [9] C. Grazianetti, G. Faraone, C. Martella, E. Bonera, A. Molle, *Nanoscale* **2019**, *11*, 18232.
- [10] W. Zhang, H. Enriquez, Y. Tong, A. Bendounan, A. Kara, A. P. Seitsonen, A. J. Mayne, G. Dujardin, H. Oughaddou, *Small* **2018**, *14*, 1804066.
- [11] J. Zhuang, C. Liu, Q. Gao, Y. Liu, H. Feng, X. Xu, J. Wang, J. Zhao, S. X. Dou, Z. Hu, Y. Du, *ACS Nano* **2018**, *12*, 5059.
- [12] E. Golias, M. Krivenkov, A. Varykhalov, J. Sánchez-Barriga, O. Rader, *Nano Lett.* **2018**, *18*, 6672.
- [13] J.-P. Xu, J.-Q. Zhang, H. Tian, H. Xu, W. Ho, M. Xie, *Phys. Rev. Mater.* **2017**, *1*, 061002.
- [14] H. Tian, J.-Q. Zhang, W. Ho, J.-P. Xu, B. Xia, Y. Xia, J. Fan, H. Xu, M. Xie, S. Y. Tong, *Matter* **2019**, *2*, 111.
- [15] S. Zhao, J. L. Zhang, W. Chen, Z. Li, *J. Phys. Chem. C* **2020**, *124*, 2024.
- [16] A. Molle, G. Faraone, A. Lamperti, D. Chiappe, E. Cinquanta, C. Martella, E. Bonera, E. Scalise, C. Grazianetti, *Faraday Discuss.* **2020**, *227*, 171.
- [17] J. L. Zhang, S. Zhao, S. Sun, H. Ding, J. Hu, Y. Li, Q. Xu, X. Yu, M. Telychko, J. Su, C. Gu, Y. Zheng, X. Lian, Z. Ma, R. Guo, J. Lu, Z. Sun, J. Zhu, Z. Li, W. Chen, *ACS Nano* **2020**, *14*, 3687.
- [18] Y. Du, J. Zhuang, J. Wang, Z. Li, H. Liu, J. Zhao, X. Xu, H. Feng, L. Chen, K. Wu, X. Wang, S. X. Dou, *Sci. Adv.* **2016**, *2*, e1600067.
- [19] A. Molle, C. Grazianetti, D. Chiappe, E. Cinquanta, E. Cianci, G. Tallarida, M. Fanciulli, *Adv. Funct. Mater.* **2013**, *23*, 4340.
- [20] J. L. Zhang, S. Zhao, M. Telychko, S. Sun, X. Lian, J. Su, A. Tadich, D. Qi, J. Zhuang, Y. Zheng, Z. Ma, C. Gu, Z. Hu, Y. Du, J. Lu, Z. Li, W. Chen, *Nano Lett.* **2019**, *19*, 5340.
- [21] C. Grazianetti, A. Molle, G. Tallarida, S. Spiga, M. Fanciulli, *J. Phys. Chem. C* **2012**, *116*, 18746.
- [22] S. M. Hus, R. Ge, P. A. Chen, L. Liang, G. E. Donnelly, W. Ko, F. Huang, M. H. Chiang, A. P. Li, D. Akinwande, *Nat. Nanotechnol.* **2021**, *16*, 58.
- [23] C. Martella, E. Kozma, P. P. Tummala, S. Ricci, K. A. Patel, A. Andicsovà-Eckstein, F. Bertini, G. Scavia, R. Sordan, L. G. Nobili, M. Bollani, U. Giovanella, A. Lamperti, A. Molle, *Adv. Mater. Interfaces* **2020**, *7*, 2000791.
- [24] T. S. Jespersen, J. Nygård, *Nano Lett.* **2005**, *5*, 1838.
- [25] C. Staii, A. T. Johnson, N. J. Pinto, *Nano Lett.* **2004**, *4*, 859.
- [26] T. Tian, D. Scullion, D. Hughes, L. H. Li, C.-J. Shih, J. Coleman, M. Chhowalla, E. J. G. Santos, *Nano Lett.* **2020**, *20*, 841.
- [27] C. Grazianetti, E. Bonaventura, C. Martella, A. Molle, S. Lupi, *ACS Appl. Nano Mater.* **2021**, *4*, 2351.
- [28] C. Martella, G. Faraone, M. H. Alam, D. Taneja, L. Tao, G. Scavia, E. Bonera, C. Grazianetti, D. Akinwande, A. Molle, *Adv. Funct. Mater.* **2020**, *30*, 2004546.